RSC Advances

PAPER

View Article Online
View Journal | View Issue

Cite this: *RSC Adv.*, 2025, **15**, 24304

Optoelectronic applications of chemical bath deposited Cu_2SnS_3 (CTS) thin films†

Jolly B. Raval, *[a] Sunil H. Chaki,*[b] Jiten P. Tailor,[c] Sandip V. Bhatt,[b] Sefali R. Patel, [e] Rahul K. Desai,[d] Bishwajit S. Chakrabarty[d] and Milind P. Deshpande[a]

Received 4th May 2025
Accepted 30th June 2025

DOI: 10.1039/d5ra03157e

rsc.li/rsc-advances

Cu_2SnS_3 (CTS) thin film (TF) is deposited by a low-cost chemical bath deposition method. The wurtzite unit cell structure of deposited CTS TF is confirmed by X-ray diffraction analysis. The atomic force microscopy shows uniform and defect-free deposition of CTS TF. The direct optical bandgap of 1.48 eV is confirmed by diffuse reflectance spectroscopy. The deposited CTS TF is studied for photo-response properties. Responsivity, sensitivity, and detectivity of 5.73 mW A^{-1}, 114.27 × 10^{-3}, and 6.39 × 10^{12} Jones are obtained respectively. In another application, the first ever heterojunction and a photo-electrochemical (PEC) type CTS-TiO_2 configuration within a single solar cell device is carried out. This CTS-TiO_2 based combined solar cell delivered a current density of 0.05 mA cm^{-2}, open circuit voltage of 0.47 V, efficiency of 0.014%, and fill factor of 0.63. Theoretical predictions of solar cell parameters for the CTS-CdX (X = S, Se) heterojunction device are carried out using SCAPS-1D simulation. Temperature-dependent thickness variations at 273, 298, 310, and 373 K are carried out to evaluate the device performance. The obtained results are discussed in detail.

1. Introduction

Quenching for renewable energy sources and finding their alternatives has become a necessity these days. The global energy crisis, such as lack of elements from the earth crust, overuse of coal and minerals, overdependence on established resources, air–water–land pollution, shortage of water, *etc.*, are leading researchers to extract better alternatives using different approaches. These alternatives involve various trendy materials that are available in different forms, such as nanoparticles (NP), thin films (TFs), single/polycrystals, *etc.* Utilization of these forms can find their practical applications in photovoltaics,[1] photocatalysts,[2] environmental and biosensors,[3,4] visible and infrared photodetectors,[5,6] *etc.* Among them, TF solar cell technology has proven to be a better substitute than the other mentioned forms.[7] The 1st generation silicon-based solar cells are extensively utilized in photovoltaic industries but some of the disadvantages that need to be addressed are indirect bandgap, high operating temperature, and time-worn use.[8,9] In the direction of addressing this, TFs of various new binary, ternary, and quaternary materials with tremendous properties are introduced every year. Conventional copper–indium–gallium–sulfur and binary cadmium-, lead-, and zinc-based chalcogenides played key role for setting directions and deliver efficient photovoltaic properties.[10] Other ternary materials such as $Cu_2Sn(S,Se)_3$,[11,12] $CuFe(S,Se)_2$,[13,14] $CuSb(S,Se)_2$,[15,16] *etc.*, are extensively synthesized due to their salient properties such as p-type conductivity,[17] high absorption coefficient,[18] significant charge carrier concentration,[19] appropriate bandgap range which is suitable for solar cells.[20] In copper-based ternary chalcogenides, Cu_2SnS_3 (CTS) is primarily employed as a p-type layer in photovoltaics because of its excellent properties such as, alterable bandgap range between 0.96 to 1.75 eV,[21] high carrier concentration,[22] existence of various crystal structures,[23] excellent electrical and thermal conductivity,[24,25] high figure of merit (*ZT*) and Seebeck coefficient.[26,27] Experimentally, the CTS TFs are deposited by various physical and chemical methods such as sputtering,[28] spin/dip coatings,[29,30] pulsed laser deposition,[31] thermal evaporation,[32] chemical bath deposition,[33] *etc.* As far as photovoltaic applications of CTS TFs are concerned, Nakshima *et al.*[34] reported solar cell efficiency (η), open circuit voltage (V_{OC}), current density (J_{SC}) and fill factor (FF) of 4.63%, 283 mV, 37.3 mA cm^{-2} and 0.439% respectively by utilizing sequential evaporation method. Kanai *et al.*[35] reported maximum η, V_{OC}, J_{SC} and FF of 5.24%, 0.25 V, 40.2 mA cm^{-2} and 0.52 respectively. As far as theoretical predictions about these solar cell parameters are concerned, the

[a]P.G. Department of Physics, Sardar Patel University, Vallabh Vidyanagar, Gujarat – 388120, India. E-mail: ravaljolly48@spuvvn.edu

[b]Department of Physics, M.B. Patel Science College, Anand, Gujarat – 388001, India. E-mail: sunil_chaki@spuvvn.edu

[c]Department of Applied & Interdisciplinary Sciences, CISST, Sardar Patel University, Vallabh Vidyanagar, Gujarat – 388120, India

[d]Department of Applied Physics, Faculty of Technology and Engineering, M.S. University of Baroda, Vadodara, Gujarat, India

[e]Department of Physics, Veer Narmad South Gujarat University, Surat, Gujarat-395007, India

† Electronic supplementary information (ESI) available. See DOI: https://doi.org/10.1039/d5ra03157e

use of SCAPS-1D software is extensively utilized these days. The software allows various parametric simulations based on material's bandgap, thickness, donor and acceptor density, electron and hole thermal velocity, and electron and hole mobility,[36] *etc.* In literature, various simulations, such as basic p–n junctions, sandwiching a perovskite layer and heterojunctions with various buffer layers with p-type CTS, demonstrated maximum predictable efficiency up to 32%.[21,37–41] As far as the n-type layer is concerned, CdS is majorly employed due to the conduction band offset of −0.1 to 0.4 eV,[42] optical bandgap of ∼2.4 eV,[43–45] stability against photo-anodic dissolution,[46] delivering efficiency in heterojunction solar cells greater than 10%,[47] tunable size and thickness in case of NPs and TFs respectively,[48,49] low resistivity,[50] *etc.* The other cadmium based chalcogenide that is widely employed is CdSe due to its n-type conductivity,[51] having direct bandgap of ∼1.71 eV,[52] higher capacity of photon absorption in the visible range,[53] high absorption coefficient of $\sim 10^4$ cm^{-1},[54] higher conduction band edge,[55] *etc.* By selecting the right p- and n-type layers for these simulations will not only deliver high theoretical device efficiency but also paves the way for experimental advancements.

In this work, the CTS TF is deposited on an FTO substrate *via* the chemical bath deposition (CBD) technique. Comprehensive characterization using X-ray diffraction (XRD), diffuse reflectance spectroscopy (DRS), and atomic force microscopy (AFM) confirmed the film's structural and optical attributes. To evaluate its multifunctional applicability, three experimental applications are employed. Initially, the photo-response behavior of CTS TF is measured with Keithley-4200 semiconductor characterization system. To the best of our knowledge, this is the first report where two fundamentally different solar cell mechanisms; hetero-junction and PEC are systematically combined in a single working device by employing a CTS-TiO_2 configuration. Finally, SCAPS-1D simulations involving FTO/CdX/CTS (X = S, Se) configurations are conducted to assess the effects of temperature and film thickness on device efficiency. Simulations are performed at temperatures of 273, 298, 310, and 373 K to identify optimal operating conditions.

This study presents a comprehensive approach by integrating experimental analysis of CTS TFs with theoretical device simulations using SCAPS-1D, bridging a gap often seen in existing literature. By exploring cost-effective Cd-based heterojunctions and assessing thermal stability across temperatures, we provide practical insights for reliable and simplified future device fabrication.

2. Experimental and characterization

The deposition of CTS TF on the fluorine doped-tin oxide (FTO) substrate is carried out by using a simple and cost-effective CBD technique. All utilized chemicals are used as received without any further purification. Prior to the deposition, the FTO is ultrasonicated in methanol for 10 min in order to remove the impurities. Cupric(II) sulphate pentahydrate ($CuSO_4 \cdot 5H_2O$) [minimum assay 99.5%, Sisco Research Laboratories (SRL) Pvt. Ltd, India], tin(II) chloride dihydrate ($SnCl_2 \cdot 2H_2O$) [minimum assay 98–103%, Himedia Laboratories Pvt. Ltd, Mumbai, India] and thioacetamide (C_2H_5NS) [minimum assay 99%, Sisco Research Laboratories (SRL) Pvt. Ltd, India] are used as a precursor sources of copper, tin and sulphur respectively. Ethylene–diamine tetra acetic acid disodium salt (Na_2–EDTA) [minimum assay 99.5%, Central Drug House (P) Ltd, Delhi, India] is used as capping agent. The needed concentrations of precursor solutions are prepared using double distilled water. In a typical deposition process, 20 ml of 0.2 M $CuSO_4 \cdot 5H_2O$ and 20 ml of 0.1 M $SnCl_2 \cdot 2H_2O$ are mixed by magnetic stirring for 30 min at 80 °C. After that, 10 ml of 0.2 M Na_2–EDTA solution is added to the prepared solution. The pH of the solution is maintained at 8.0 by adding 10 ml aqueous ammonia solution. After that, 20 ml of 0.3 M C_2H_5NS solution is added to the above solution. The mixture is stirred for 5 min and transferred to water bath for 4 h at 90 °C and allowed to remain still. In still condition, a pre-cleaned substrate is dipped vertically into the solution for film deposition. After 4 h, the substrate having the film is taken out and given multiple wash with water and methanol. After thorough wash, the deposited TF is annealed at 150 °C for 4 h. Fig. S1† shows the schematic diagram of deposition of CTS TF by CBD method. The crystal structure of deposited CTS TF is confirmed by XRD using Rigaku Ultima IV X-ray diffractometer. The optical properties of deposited CTS TF are studied employing DRS using Lambda 19, PerkinElmer, USA. Uniformity of as deposited CTS TF is confirmed by AFM.

3. Results and discussion

3.1. XRD

Fig. 1 displays the XRD pattern of the deposited CTS TF, confirming its wurtzite lattice structure. A few low-intensity peaks associated with Sn_2S_3 and Cu_2S suggest the incorporation of minor secondary phases during film formation.[56] The deposited CTS TF has orientations along (100), (002), (101), (102), (110), (103) and (112) planes at different 2θ angles.

The average crystallite size of deposited CTS TF is determined employing Scherrer's equation,[57]

$$D = \frac{K \times \lambda}{\beta \cos \theta} \quad (1)$$

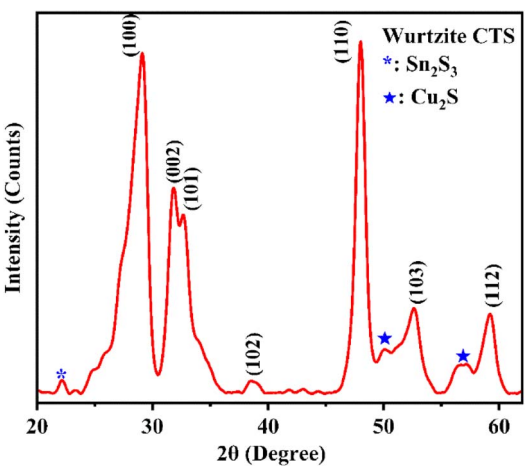

Fig. 1 The XRD pattern of deposited CTS TF.

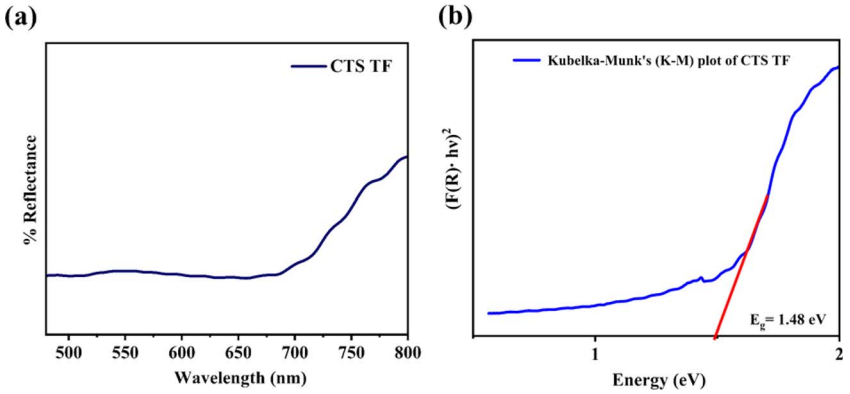

Fig. 2 The (a) diffuse reflectance spectrum, and (b) K–M plot of CTS TF.

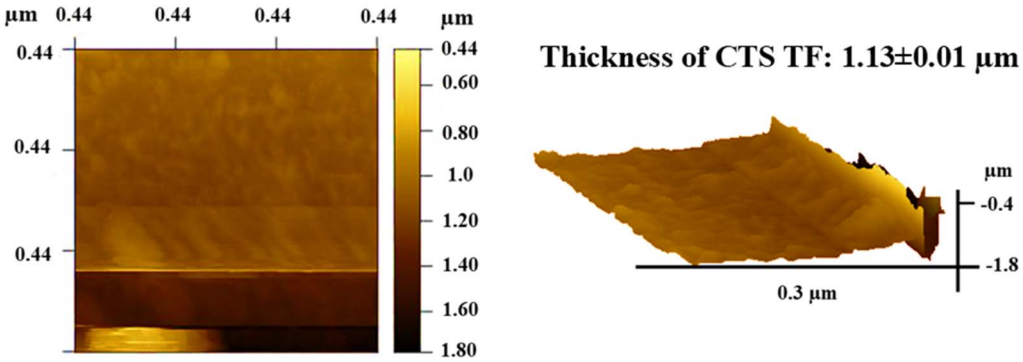

Fig. 3 The (a) 2D and (b) 3D AFM images of CBD deposited CTS TF.

Here, D represents the average crystallite size, λ is the wavelength of the Cu-Kα X-ray radiation (1.5408 Å), β denotes the full width at half maximum (FWHM), and K is the Scherrer's constant, which depends on factors such as shape, size distribution, diffraction line indices, and the definition adopted for the calculation,[58] and θ is Bragg angle. The constant K in the Scherrer equation varies between 0.62 and 2.08 based on material characteristics. In this work, a standard value of 0.94 has been selected. The peak broadening parameter β is highly sensitive to internal micro strains and local compositional inhomogeneities.[59] The estimated average crystallite size of deposited CTS TF using the above eqn (1) is 87.85 nm.

3.2. DRS

The DRS of the CTS TF, shown in Fig. 2(a), reveals an absorption edge around 677 nm, confirming its visible light absorption. Fig. 2(b) illustrates the Tauc plot based on the Kubelka–Munk function to determine the band gap energy.

An estimation of bandgap of deposited CTS TF is carried out by employing following equation,[60]

$$(F(R)\cdot h\nu)^{1/n} = A(E_g - h\nu) \quad (2)$$

Where, $F(R)$ is K–M function, $h\nu$ is photon energy and $n = 2$. The Tauc plot along with K–M function estimates the direct optical bandgap of 1.48 eV, which is in good agreement with the reported bandgap range for CTS (0.93–1.75 eV).[21]

3.3. AFM

Fig. 3(a and b) depicts the 2D and 3D AFM images of CBD deposited CTS TF. The AFM images suggest uniform distribution along with development of small grains.

AFM images indicate uniform growth and well-distributed nucleation of the CTS thin film during the CBD process. The film thickness is measured using the gravimetric method.[61] The thickness of the deposited films is 1.13 ± 0.01 µm. The R_q and R_{rms} values of deposited CTS TF are 20.42 ± 5.03 nm and 27.45 ± 7.55 nm respectively which is well matched with previous reports.[60,61]

4. Experimental and theoretical applications of CTS TF

The following sections explore different optoelectronic applications of the CTS TF, with a comprehensive analysis of the results. The first application focuses on evaluating the photoresponse characteristics of the deposited film. For this, the photo-response of a CTS layer is evaluated under a light intensity of 50 mW cm^{-2} and device parameters such as responsivity, detectivity, sensitivity and photocurrent is determined. In the

second application, first ever combined hetero and PEC type CTS-TiO_2 solar cell configuration is proposed. TiO_2 is selected as the n-type layer due to its widespread use and favorable electronic properties in solar cell.[62] To overcome limitations observed during the experimental fabrication of CTS-TiO_2 based PEC solar cells, a theoretical model is proposed. In which, heterojunction of CTS layer with Cd based chalcogenides is proposed. In this, alternative n-type layers such as CdS and CdSe are integrated into CTS-CdX configurations and simulated using SCAPS-1D. The simulations further explore the influence of temperature on device performance, with calculations performed for 273, 298, 310, and 373 K. This comprehensive study, combining experimental investigation, device application, and theoretical simulation, highlights the viability of CTS-based materials for future optoelectronic and solar energy applications.

4.1. Photo-response properties of deposited CTS TF

The device configuration for evaluating the photo-response properties of deposited CTS TF is shown in Fig. S2.† The photo-response of the CTS thin film is tested by attaching copper wires with silver paste. One end of each wire is connected to the film, and the other end is soldered to a PCB board to complete the measurement setup. To maintain stable electrical contacts during the measurement process the copper wires are fixed to the PCB with glue. The wire-to-film connections, made using silver paste, are heated under an incandescent lamp to improve their conductivity and achieve ohmic contact. These connections are then interfaced with the Keithley-4200 semiconductor characterization system for performance evaluation.

Fig. 4(a and b) shows the current–voltage (*I–V*) characteristics under both dark and white light illumination and the photocurrent *versus* voltage plot of deposited CTS TF, respectively.

The linearity observed in the *I–V* plots under dark and light conditions, shown in Fig. 4(a), confirms the ohmic nature of the contacts on the deposited CTS TF. Under light illumination with intensity of 50 mW cm^{-2}, the current increased due to the photo-generation of charge carriers. As the light is incident on the deposited CTS TF, the concentration of charge carriers increases, leading to an increase in photocurrent depicted in Fig. 4(b). The derivation of photo-response parameters such as photocurrent (I_{ph}), sensitivity (S), responsivity (R), and detectivity (D) in response to applied voltages is done employing the below equations;[63]

$$I_{ph} = I_{light} - I_{dark} \quad (3)$$

$$S = \frac{I_{ph}}{I_{dark}} \quad (4)$$

$$R = \frac{I_{ph}}{P \times A} \quad (5)$$

$$D = \frac{R \times A^{1/2}}{(2e \times I_{dark})^{1/2}} \quad (6)$$

where; I_{ph} is photocurrent, P is incident light intensity (50 mW cm^{-2}), e is charge of an electron (1.6×10^{-19} C) and A is area of illumination (1.0 cm^2). Table 1 shows the calculated photo-response parameters of deposited CTS TF.

The Table 2 shows the comparative analysis of reported photo-response properties of CTS in different forms.

The photo-response parameters of Tables 1 and 2 shows enhanced photocurrent and improved detectivity in present CTS TF, demonstrating excellent photo-response of deposited CTS TF.

4.2. Fabrication of CTS-TiO_2 based photo-electrochemical (PEC) type solar cell

In this study, a photoelectrochemical (PEC) solar cell based on a CTS-TiO_2 heterojunction is fabricated. A PEC solar cell operates through a semiconductor–electrolyte interface, where photo-generated charge carriers are collected *via* electrodes.[69] CTS has been identified as a suitable candidate for photovoltaic applications owing to its intrinsic p-type conductivity, tunable bandgap within the range of 0.93 to 1.75 eV, high carrier density, and significant optical absorption.[70,71] On the other

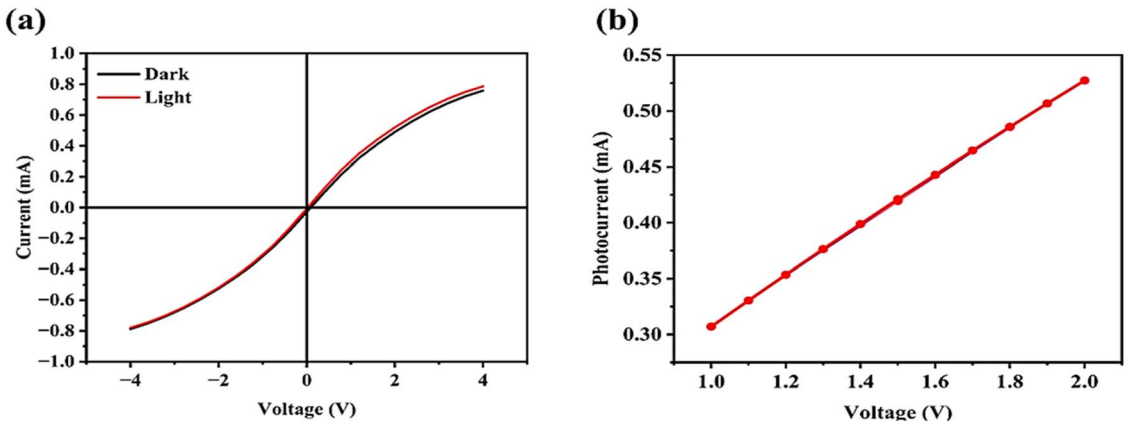

Fig. 4 The (a) *I–V* characteristics under both dark and white light illumination having intensity of 50 mW cm^{-2} and (b) photocurrent *versus* voltage plot of deposited CTS TF.

Table 1 Photo-response parameters of deposited CTS TF

Material name	Bias voltage (V)	I_{ph} (μA)	R (mA W^{-1})	S	D (Jones)	Light source
CTS TF	1.0	28.67	5.73	114.27×10^{-3}	6.39×10^{12}	Visible light

Table 2 Comparative analysis of photo-response properties of CTS in different forms[a]

No.	CTS	Configuration	D	R	Ref.
1	TF (co-evaporation)	Glass/CTS/Ag	24×10^{6}	0.14 (A W^{-1})	64
2	TF (spin coating)	SLG/CTS/Ag	5.10×10^{10}	16.32 (mA W^{-1})	65
3	Nanostructures (solvothermal)	PET/ITO/PEDOT:PSS[a]	8.7×10^{9}	211.5 (mA W^{-1})	66
4	TF (D.C. sputtering)	SLG/Mo/CTS/CdS, ZnO/GIZnO	3.9×10^{12}	552.3 (A W^{-1})	67
5	CTS (QD)	SLG/ITO/CTS QD/Ag	2.79×10^{11}	1.76 (A W^{-1})	66
6	CTS (QD)	SLG/ITO/CTS QD/Ag	2.11×10^{10}	7.66 (mA W^{-1})	68
7	CTS (CBD)	FTO/CTS/Ag	6.39×10^{12}	5.73 (mA W^{-1})	Present work

[a] Poly(3,4 ethylenedioxythiophene):poly(styrenesulfonate).

side, TiO_2 is used as a potent heterojunction material due to n-type conductivity, a suitable bandgap range of 3.0 to 3.3 eV depending upon various phases, enhanced electron transfer, stability under visible light illumination, and nontoxicity.[72,73]

A two-electrode solar cell configuration is developed in this work. The working electrode consisted of a CTS-TiO_2 heterojunction formed on an FTO substrate, with CTS and TiO_2 layers deposited using CBD and dip-coating techniques, respectively. The electrode is then annealed at 100 °C for 4 h to facilitate better interfacial contact and structural integrity. The second electrode is a graphite electrode prepared by simply rubbing the pencil on the FTO substrate. The electrolyte solution is prepared by dissolving 0.127 g of iodine (I_2) in 10 ml of ethylene glycol, followed by the addition of 0.831 g of potassium iodide (KI), and stirring the mixture for 7 min. The cell fabrication is done by sandwiching prepared iodine electrolyte between the two above-prepared electrodes. The analysis of device parameters is carried out by the Keithley 4200 semiconductor characterization system by measuring I–V measurements. Fig. 5(a and b) shows the picture of the prepared device and the I–V plot of CTS-TiO_2 PEC type solar cell, respectively.

The calculation of solar cell parameters is done by employing following equations;[74]

$$\text{Fill factor (FF)} = \frac{V_m \times J_m}{V_{OC} \times J_{SC}} \quad (7)$$

$$\eta = \text{FF} \times \frac{V_{OC} \times J_{SC}}{P_{in}} \quad (8)$$

Table 3 shows the obtained solar cell parameters of CTS-TiO_2 PEC type solar cell.

The Table 3 data states the J_{SC}, V_{OC}, and FF of the prepared CTS-TiO_2 cell is low compared to the other reported solar cells based on CTS.[75–77] The integration of heterojunction and PEC mechanisms introduces conceptual novelty, their opposing photoresponses create an internal conflict in charge carrier dynamics, leading to poor device performance. Several other factors may be responsible for the present lower values of

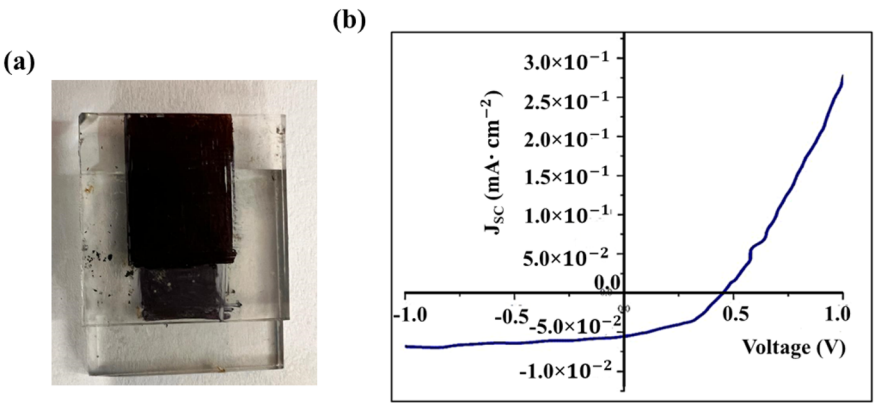

Fig. 5 The (a) fabricated device and (b) I–V plot of CTS-TiO_2 PEC type solar cell.

Table 3 Solar cell parameters of CTS-TiO_2 PEC type solar cell

V_{OC} (V)	J_{SC} (mA cm^{-2})	η (%)	FF (%)
0.470	0.05	0.014	0.63

photovoltaic parameters in this combined solar cell. These limitations of deposition techniques, inefficient charge transfer, small surface area, poor absorber layer quality, leakage currents, unfavorable series/shunt resistance, high recombination rates, and intrinsic material defects.[78]

4.3. Temperature dependent thickness variations of CTS-CdX (X = S, Se) cell using SCAPS-1D software

Based on the experimental findings, theoretical simulations are conducted to further explore device performance by combining CTS with cadmium-based chalcogenides, replacing TiO_2 used in the experimental setup. The experimentally measured thickness (1.13 ± 0.01 μm) and bandgap (1.48 eV) closely match the literature values,[75,79,80] thereby supporting the validity of the parameters used in the simulations. Total 32 device simulations based on different thickness and temperature conditions are carried out.

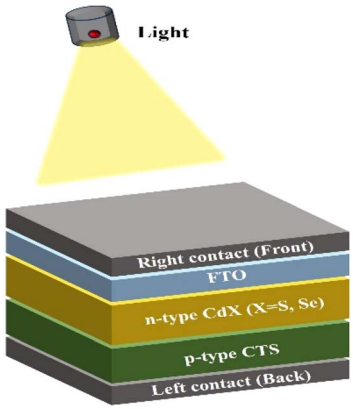

Fig. 6 Schematic diagram of proposed device structure.

In this section, theoretical simulation of a CTS-CdX heterojunction solar cell is carried out using SCAPS-1D simulation software. Very basic device configuration CTS/CdX/FTO is employed for all the simulations. The authors performed thickness variations at different temperatures of 273, 298, 310, and 373 K in order to analyze the effect of temperature on various solar cell parameters such as V_{OC}, J_{SC}, η (%), and FF. Fig. 6 shows the schematic diagram of the proposed device structure.

In the thickness variations, the thickness of the p-type CTS layer is varied from 1 to 4 μm. The thicknesses of n-type CdS and CdSe layers are set to their optimum value based on the experimentally reported range of thickness possible by various deposition methods.[44,45,81–83] All simulations are undertaken for 1.5 global air mass (AM) sun illuminations (1000 W m^{-2}). The simulated parameters of CTS-CdX device are summarized in Table 4.

4.3.1. Thickness variations in CTS-CdS device. Fig. 7(a–d) shows the current density (J) *versus* voltage (V) plots of the CTS-CdS device for temperatures of 273, 298, 310, and 373 K. The thickness of the CTS layer varies between 1 to 4 μm by keeping the optimum thickness of 2.0 μm of the n-type CdS layer based on reported experimental thickness achieved by various physiochemical methods.[44,45,81–83] Bandgaps of CTS and CdS layer are 1.00 eV and 2.40 eV respectively.[50,84–87]

The V_{oc} and J_{sc} variation with thickness for different temperatures of 273, 290, 310 and 398 K are given in below Table 5.

The data shows the V_{oc} and J_{sc} decreases with a rise in temperature and increase with the thickness of CTS layer. The deterioration is due to an increase in phonon with temperature

Table 4 The simulation parameters of CTS-CdX device

Simulation parameters	p-CTS	n-CdS	n-CdSe	FTO
Thickness (μm)	1 to 4[a] μm	2.0 μm	2.0 μm	1 μm
Bandgap (eV)	1.0	2.40 eV	1.71	3.6 eV
Electron affinity (eV)	4.5	4.5	4.5	4.5
Dielectric permittivity (relative)	10.00	10.00	10.00	10.00
CB effective density of states (1 cm^{-3})	1×10^{19}	1×10^{19}	1×10^{19}	1×10^{19}
VB effective density of states (1 cm^{-3})	1×10^{19}	1×10^{19}	1×10^{19}	1×10^{19}
Electron thermal velocity (cm s)	1×10^{7}	1×10^{7}	1×10^{7}	1×10^{7}
Hole thermal velocity (cm s)	1×10^{7}	1×10^{7}	1×10^{7}	1×10^{7}
Electron mobility (cm^2 V s)	5×10^{1}	5×10^{1}	5×10^{1}	5×10^{1}
Hole mobility (cm^2 V s)	5×10^{1}	5×10^{1}	5×10^{1}	5×10^{1}
Shallow uniform donor density (N_d) (1 cm^{-3})	1×10^{19}	1.1×10^{17}	1.1×10^{20}	2.2×10^{18}
Shallow uniform acceptor density (N_a) (1 cm^{-3})	1×10^{20}	1.1×10^{8}	1.1×10^{10}	1.1×10^{18}
Radiative recombination coefficient (cm^3 s)	0.00	0.00	0.00	0.00
Contact parameters				
Front and back contact				
Flat band condition				
Surface recombination velocity of hole:1.0×10^{5} cm s^{-1}				
Surface recombination velocity of electron:1.0×10^{7} cm s^{-1}				

[a] Variable property.

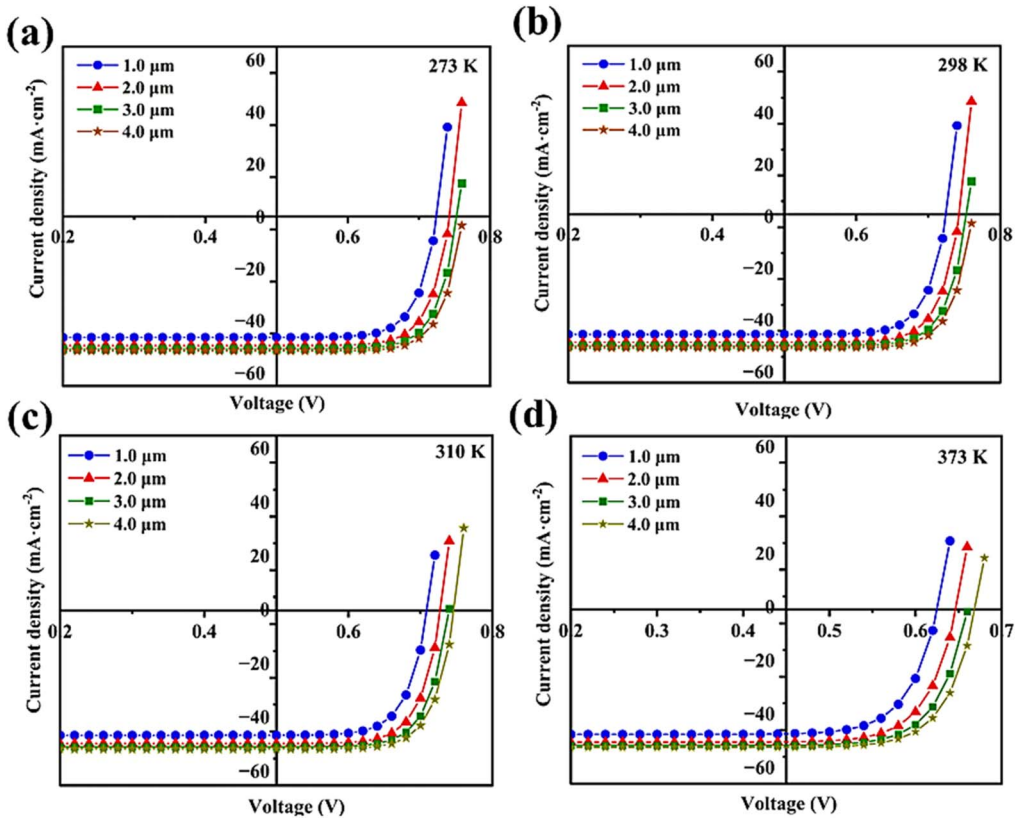

Fig. 7 The *J versus V* plots of CTS-CdS device at (a) 273, (b) 298, (c) 310, and, (d) 373 K.

Table 5 The obtained V_{OC} and J_{SC} values of CTS-CdS for different thicknesses and temperatures

	Temperature (K)							
	273		298		310		373	
CTS thickness (μm)	V_{OC} (V)	J_{SC} (mA cm^{-2})	V_{OC} (V)	J_{SC} (mA cm^{-2})	V_{OC} (V)	J_{SC} (mA cm^{-2})	V_{OC} (V)	J_{SC} (mA cm^{-2})
1	0.721	41.0	0.720	41.0	0.703	40.8	0.623	41.5
2	0.743	43.7	0.743	43.5	0.722	44.5	0.641	44.5
3	0.751	44.5	0.751	44.3	0.731	45.0	0.651	45.0
4	0.752	46.5	0.752	46.1	0.740	46.7	0.661	46.5

in the cell materials. So, low-temperature operation of solar cells is desirable. The cumulative changes in both the values indicate that by providing basic device structure, one can predict the simplest solar cell with significant device characteristics. Fig. 8(a) shows the plots of V_{OC} variation with thickness of CTS for different temperatures. It is clearly observed that as the temperature increases, V_{oc} value decreases. The efficiency *versus* CTS layer thickness is shown in Fig. 8(b). This also shows the efficiency deteriorating with temperature. Fig. 8(c) shows the efficiency variation with temperature for a CTS thickness of 4 μm. The efficiency continuously decreases with a rise in temperature.

As shown in Fig. 8(a–c), the efficiency rises with CTS layer thickness but drops with increasing temperature. The CTS-CdS device demonstrates its best performance at 273 K and for 4 μm thick layer.

4.3.2. Thickness variation in CTS-CdSe device. Fig. 9(a–d) shows the current density *versus* voltage plot of the CTS-CdSe device for temperatures of 273, 298, 310, and 373 K. The thickness of the n-type CdSe layer is kept constant at 2.0 μm based on the reported experimental thickness of the CdSe layer.[82] Bandgaps of CTS and CdSe layer are kept 1.0 and 1.71 eV respectively.[87]

The V_{oc} and J_{sc} values for different thicknesses and different temperatures of CTS-CdSe devices are tabulated in Table 6.

Fig. 10(a and b) shows the comparative plots of V_{OC} and efficiency η *versus* thickness of the CTS layer at different temperatures. The Fig. 10(c) shows efficiency η *versus* temperature for fixed CTS thickness of 4 μm.

All the above characteristic plots are of similar nature to that of the CTS-CdS device. The V_{OC} and efficiency values showed an increase with thickness, whereas it illustrates a decreasing trend

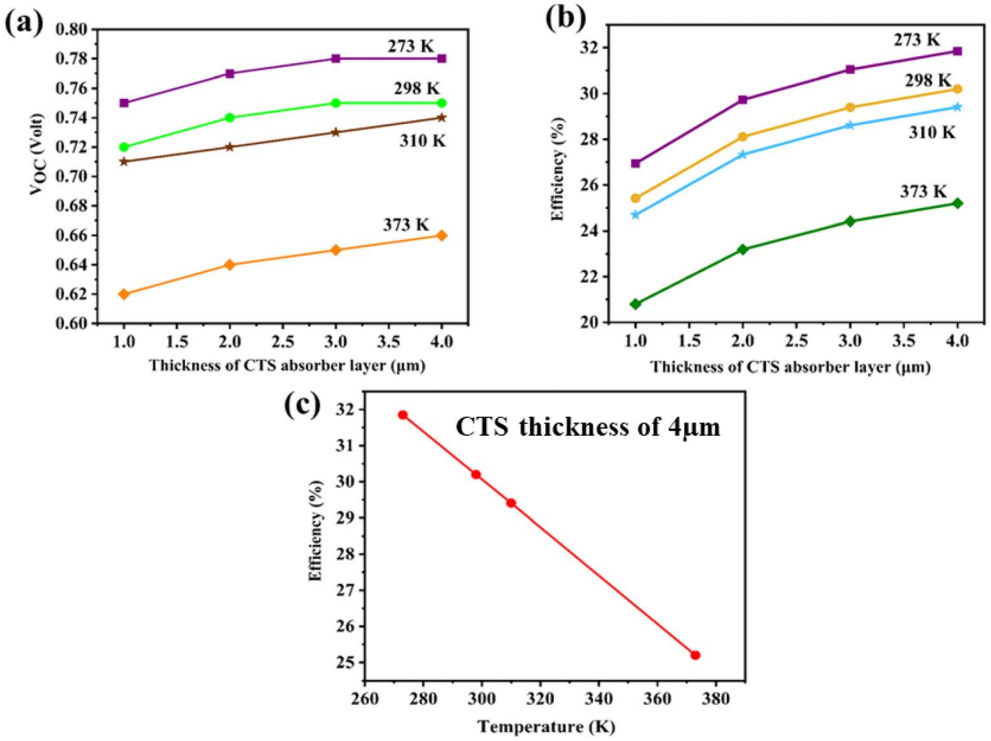

Fig. 8 Comparative plots of (a) V_{OC} *versus* thickness of CTS layer with variation of temperature, (b) efficiency (η) *versus* thickness of CTS layer with temperature variation, and (c) efficiency (η) *versus* temperature (K) for fixed CTS thickness of 4 μm.

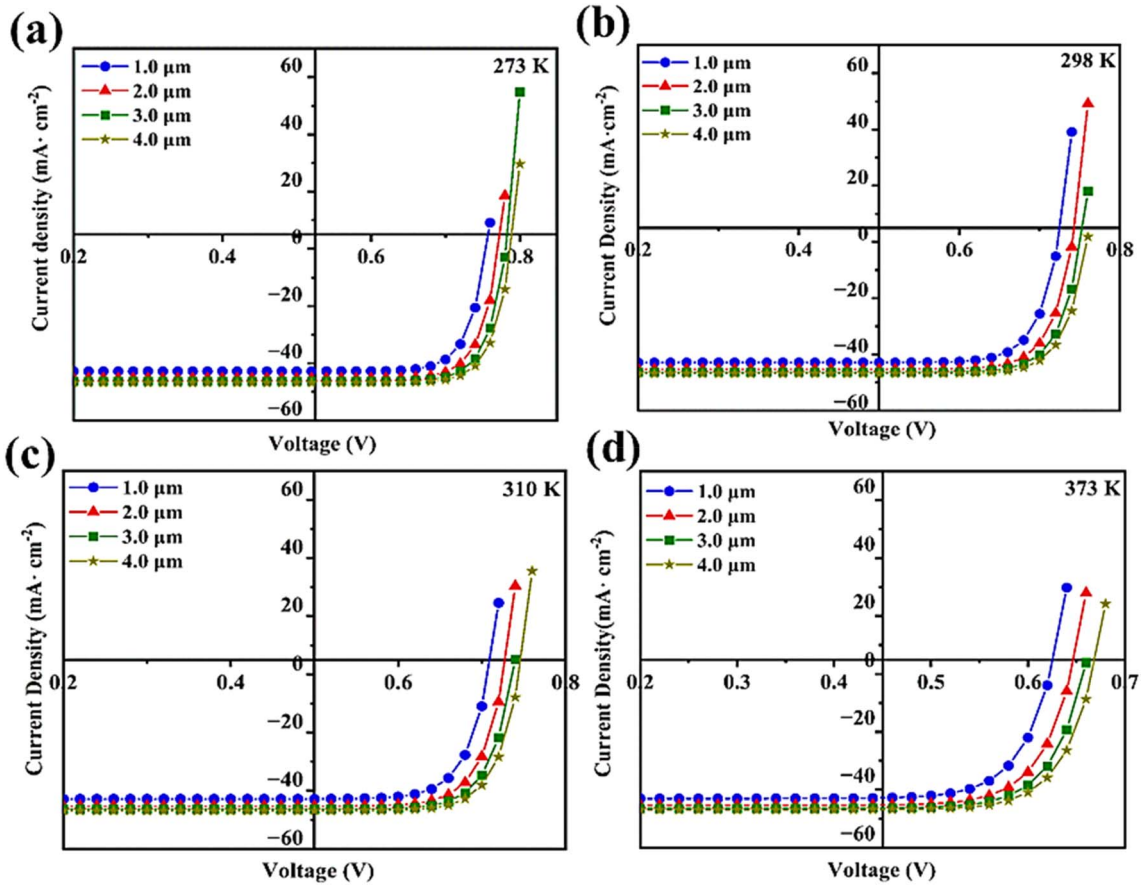

Fig. 9 The *J versus V* plots of CTS-CdSe devices at temperatures of (a) 273, (b) 298, (c) 310 and (d) 373 K.

Table 6 The obtained V_{OC} and J_{SC} values of CTS-CdSe for different thicknesses and temperatures

	Temperature (K)							
	273		298		310		373	
CTS thickness (μm)	V_{OC} (V)	J_{SC}(mA cm^{-2})	V_{OC} (V)	J_{SC} (mA cm^{-2})	V_{OC} (V)	J_{SC} (mA cm^{-2})	V_{OC} (V)	J_{SC} (mA cm^{-2})
1	0.753	43.2	0.721	42.1	0.700	42.6	0.621	42.4
2	0.771	44.1	0.742	43.9	0.721	43.9	0.644	43.7
3	0.782	45.6	0.750	45.4	0.740	45.2	0.660	46.3
4	0.780	47.0	0.753	46.7	0.744	46.7	0.664	45.3

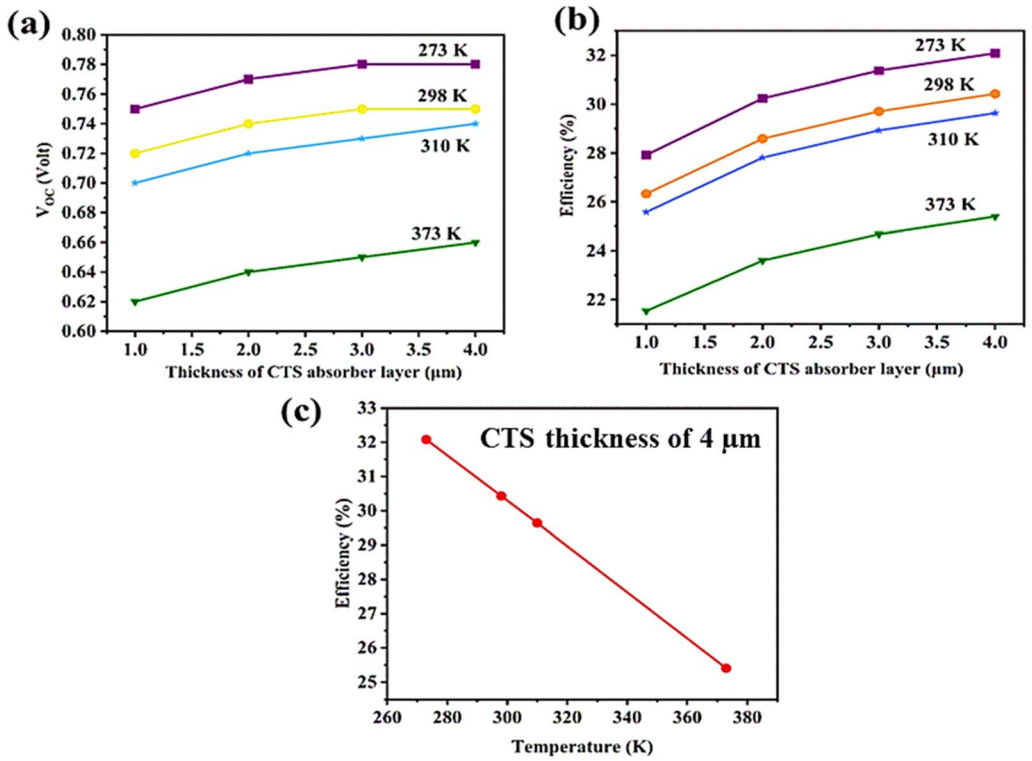

Fig. 10 Plots of (a) V_{OC}, (b) efficiency (η) as a function of CTS absorber layer thickness at different temperatures and (c) efficiency (η) as a function of tempeature (K) for 4 μm thickness CTS layer.

with temperature. The overall efficiency of the proposed CTS-CdSe device decreases with temperature increase. At 273 K, the proposed CTS-CdSe device delivered a maximum efficiency of 32.08% for a CTS layer thickness of 4 μm. Thus, the CTS layer, having a thickness of 4 μm and an operating temperature of 273 K, is considered an optimum for excellent device parameters. Tables S1 and S2† shows the average and standard deviation calculation of obtained results from CTS-CdS and CTS-CdSe devices respectively.

5. Parametric influences on the experimental and simulated performance of CTS-TiO_2 and CTS-CdX devices

Experimentally, the effective suppression of electron–hole recombination is essential for enhancing the stability, efficiency, and durability of the fabricated photovoltaic device.[88] In the present study, CTS exhibits a high carrier concentration in the range of ~10^{18}–10^{19} cm^{-3}.[89] Such a high density of charge carriers increases the probability of electron–hole recombination within the material. In addition, defects in the crystal lattice can act as trap states, promoting charge carrier recombination and reducing device efficiency.[90] Poor adhesion of the CTS thin film to the substrate can hinder device efficiency; therefore, adopting an alternative deposition approach and optimizing related parameters may yield improved film quality and performance.[31] In CBD, both deposition time and temperature are vital parameters that dictate CTS film uniformity and thickness. The deposition temperature and time significantly affects the structural integrity, while the bath temperature governs the crystallinity of the resulting thin films.[91,92] Various other physical deposition techniques such as sputtering, thermal evaporation, and spray pyrolysis offers advantages over

Table 7 Comparative analysis of solar cell parameters employing various configurations using SCAPS-1D

No.	Device configuration	E_g (CTS) (eV)	Thickness (CTS) (μm)	Solar cell parameters				Ref.
				J_{SC} mA cm^{-2}	V_{OC} (V)	η (%)	FF (%)	
1	iZnO/CdS/p-CTS	1.25	4.0	35.0	0.712	20.3	—	110
2	p-CTS/n-CdS/i-ZnO/n-ZnO:Al	0.91	2.5	48.6	0.580	22.3	78.09	111
3	ITO/ZnSe/CTS/Cu_2O/Au	1.21	0.4	37.2	0.940	30.0	86.87	38
4	n-ZnSe/p-CTS	—	—	32.3	0.602	17.6	80.58	39
5	Al/n-ZnO:Al/i-ZnO/n-CdS/p-CTS/Mo/SLG	0.96	1 to 4	>24.0	0.703	12.0	0.3 to 0.8	112
6	SLG/Mo/CTS/ZnS/ITO/Al	—	—	24.6	1.091	20.3	75.23	21
7	FTO/CdS/CTS	1.0	4.0	~46.5	~0.720 to 0.753	31.8	86.88	Present work
8	FTO/CdSe/CTS	1.0	4.0	~47.1	~0.750 to 0.781	32.0	86.90	Present work

CBD by ensuring better film-substrate adhesion and more consistent thickness, which are key to achieving reliable and efficient device operation over longer time span.[32,93,94] To enhance photovoltaic performance, CTS can be paired with diverse n-type materials such as ZnS, CdS, CdSe, ZnO, or perovskite systems based on $CH_3NH_3(Sn,Pb)(Br,I)_3$, which have shown promising efficiencies nearing 20% in reported studies.[53,95–97]

While desinging the device in software, device parameters such as back and front contacts, metal work functions, HOMO and LUMO levels, donor and acceptor density of the materials, temperature, bandgap of the material, thickness of the absorber layer, interface properties of layers, defect densities, charge carrier lifetime, *etc.*, are considered key parameters that deeply affect the V_{OC}, J_{SC}, and η.[98] In the present case of the CTS-CdX device, as the thickness of the CTS absorber layer is increased from 1 to 4 μm, the photon absorption increases, leading to enhanced current density, thus augmenting efficiency and fill factor.[98] Elevation of recombination rate in any layer depends upon the optimum thickness of that layer.[38] Determination of the optimum CTS layer thickness depends upon several factors, such as bandgap range (0.96–1.75 eV),[99] experimental deposition conditions (pH, temperature, adhesion),[100] high absorption coefficient ~10^5 cm^{-1},[38,101] *etc.* The device response of the CTS-CdX configuration is found to decrease as the temperature increases from 273 to 373 K. As the temperature increases, the phonon contribution increases, leading to hindrance to carrier flow, thus decreasing the voltage and output power of the CTS-CdX device.[98] Parameters such as ohmic loss, which consists of series and shunt resistances, recombination loss, reverse saturation current, reduction loss, *etc.*, are also responsible for the drastic changes in V_{OC}, J_{SC}, and efficiency of the device. Singh et *al.*[102] demonstrated that the reverse saturation current density (J_0) which arises due to minority charge carriers which affects the overall performance of the device. The equation of J_0 is given as follow;[102,103]

$$J_0 = q \times \left(\frac{D_n}{L_n \times N_a} + \frac{D_p}{L_p \times N_D} \right) \times n_i^2 \quad (9)$$

where, n_i is the intrinsic carrier density, N_A and N_D are acceptor and donor densities, respectively, D_n and D_p are diffusion constants in p- and n-regions, respectively, and L_n and L_p are the diffusion lengths of minority charge carriers in p- and n-regions, respectively. The trend observed in all the simulations reveals that increasing CTS layer thickness improves all parameters for 273, 298, 310, and 373 K, but the overall response decreases as temperature rises. The proposed CTS-CdX device delivered enhanced V_{OC} and efficiency at lower temperatures of 273 and 298 K compared to the higher ones. As per eqn (9), the J_0 is directly related to the minority charge carriers, which are thermally generated[104,105] and are responsible for the enhanced V_{OC} and efficiency at lower temperature. At 273 and 298 K, these minority charge carriers move slowly so that they have sufficient time to interact. With the lowest temperature of 273 K in the proposed CTS-CdX device, the reduction in intrinsic carrier density occurred, which is responsible for the enhanced V_{OC}.[106]

In both theoretical and experimental fabrication of CTS-based heterojunction solar cells, interfacial properties play a pivotal role. Imperfections or energy misalignments at the interfaces where CTS is sandwiched can create recombination centers, thereby lowering the V_{OC} and J_{SC} values of the device.[107] At the interface, the presence of defects acts as the trapping sites, which trap the charge carriers and prevent them from reaching the electrode. Rapid recombination at trap sites limits charge carrier collection, resulting in lower current and poor cell efficiency.[108,109]

Table 7 shows the comparative analysis of solar cell parameters reported for various configurations using SCAPS-1D.

The analysis of the parameters of Table 7 clearly shows that the present configuration studied by authors has potential for device improvements experimentally by involving the CTS material.

6. Conclusion

The CTS thin film, synthesized using the CBD technique, exhibited a wurtzite crystalline phase as identified by XRD. Surface morphology assessments *via* AFM confirmed a uniform and well-distributed film on the FTO substrate. Optical characterization through DRS and the Kubelka–Munk approach indicated visible-range absorption and a direct bandgap of 1.48 eV. These findings qualified the film for use in multiple optoelectronic applications, such as light-response

measurements, PEC solar cell fabrication, and theoretical simulations with SCAPS-1D. The deposited CTS thin film was analyzed for its photo-response behaviour under both dark and illuminated conditions. An increase in photocurrent was observed as the bias voltage was raised from 1 V to 2 V. At 1 V bias, the CTS TF demonstrated a responsivity of 5.73 mA W^{-1}, a sensitivity of 114.27 $\times$ 10^{-3}, and a detectivity of 6.39 $\times$ 10^{12} Jones, indicating its promising potential for optoelectronic applications. In another application, the PEC CTS-TiO_2 solar cell exhibited a current density of 0.05 mA cm^{-2}, an open-circuit voltage of 0.470 V, an efficiency of 0.014%, and a fill factor of 0.63. Although the obtained efficiency is found to be low, this hybrid operation opens up new possibilities for dual-mode solar cell configurations, particularly in next-generation energy conversion systems. To overcome the relatively low efficiency observed in experimental PEC solar cells, theoretical simulations are conducted using SCAPS-1D. Here, TiO_2 was replaced with CdX (X = S, Se) as the n-type layer to examine the impact on device performance. The proposed device CTS-CdX (X = S, Se) works excellently at 273 K and moderately at 310 K. Furthermore, an increase in temperature is observed to negatively impact the overall device performance. To achieve higher efficiencies in practical applications, it is essential to focus on fine-tuning intrinsic parameters such as charge carrier dynamics, interface recombination, and band alignment. These factors directly influence the voltage output and energy conversion capability of the device and represent vital targets for future research. This can be achieved by controlling operating temperature, hole–electron mobility, and thermal velocity, sandwiching various perovskite layers, and making heterojunctions of compounds such as ZnX (X = S, Se, and Te), ZnO, PbO, PbX (X = S, Se, and Te), *etc.* Given their promising experimental and theoretical performance, CTS-based devices emerge as strong candidates for replacing traditional silicon and germanium counterparts in next-generation solar technologies.

Data availability

The data included in this manuscript is completely carried out by the authors.

Conflicts of interest

There is no conflict of interest to declare for this work.

Acknowledgements

The authors of this manuscript are sincerely thankful to Prof. M. Burgelman and his team at University of Ghent, Belgium for providing the SCAPS-1D simulation software. The authors are also thankful to Dr Jayesh Gandhi for XRD, Sophisticated Instrumentation Centre for Applied Research and Testing (SICART) for DRS and Dr SaurabhS.Soni, P.G. Department of Chemistry, Sardar Patel University for AFM.

References

1 M. Ravindiran and C. Praveenkumar, *Renewable Sustainable Energy Rev.*, 2018, **94**, 317–329.
2 G. K. Weldegebrieal, *Inorg. Chem. Commun.*, 2020, **120**, 108140.
3 L. Wang, W. Ma, L. Xu, W. Chen, Y. Zhu, C. Xu and N. A. Kotov, *Mater. Sci. Eng., R*, 2010, **70**, 265–274.
4 P. P. Li, X. P. Liu, C. J. Mao, B. K. Jin and J. J. Zhu, *Anal. Chim. Acta*, 2019, **1048**, 42–49.
5 G. Konstantatos, J. Clifford, L. Levina and E. H. Sargent, *Nat. Photonics*, 2007, **1**, 531–534.
6 K. Ramakrishnan, B. Ajitha and Y. A. K. Reddy, *Sens. Actuators, A*, 2023, **349**, 114051.
7 T. D. Lee and A. U. Ebong, *Renewable Sustainable Energy Rev.*, 2017, **70**, 1286–1297.
8 M. A. Green, in *Seventh EC Photovoltaic Solar Energy Conference*, Springer, 1987, pp. 681–687.
9 T. Matsui, H. Sai, A. Bidiville, H.-J. Hsu and K. Matsubara, *Sol. Energy*, 2018, **170**, 486–498.
10 V. Kumar, R. Prasad, N. B. Chaure and U. P. Singh, in *Recent Advances in Thin Film Photovoltaics*, Springer, 2022, pp. 5–39.
11 R. Garza-Hernández, H. J. Edwards, J. T. Gibbon, M. R. Alfaro-Cruz, V. R. Dhanak and F. S. Aguirre-Tostado, *J. Alloys Compd.*, 2021, **881**, 160552.
12 H. Ming, G. Zhu, C. Zhu, X. Qin, T. Chen, J. Zhang, D. Li, H. Xin and B. Jabar, *ACS Nano*, 2021, **15**, 10532–10541.
13 Y.-H. A. Wang, N. Bao and A. Gupta, *Solid State Sci.*, 2010, **12**, 387–390.
14 J. M. Delgado, G. D. De Delgado, M. Quintero and J. C. Woolley, *Mater. Res. Bull.*, 1992, **27**, 367–373.
15 B. Yang, L. Wang, J. Han, Y. Zhou, H. Song, S. Chen, J. Zhong, L. Lv, D. Niu and J. Tang, *Chem. Mater.*, 2014, **26**, 3135–3143.
16 D. Xue, B. Yang, Z. Yuan, G. Wang, X. Liu, Y. Zhou, L. Hu, D. Pan, S. Chen and J. Tang, *Adv. Energy Mater.*, 2015, **5**, 1501203.
17 Y. Shen, C. Li, R. Huang, R. Tian, Y. Ye, L. Pan, K. Koumoto, R. Zhang, C. Wan and Y. Wang, *Sci. Rep.*, 2016, **6**, 32501.
18 A. Rabhi, M. Kanzari and B. Rezig, *Thin Solid Films*, 2009, **517**, 2477–2480.
19 J. Navrátil, P. Levinský, J. Hejtmanek, M. Pashchenko, K. Knížek, L. Kubíčková, T. Kmječ and C. Drašar, *J. Phys. Chem. C*, 2020, **124**, 20773–20783.
20 R. Chierchia, F. Pigna, M. Valentini, C. Malerba, E. Salza, P. Mangiapane, T. Polichetti and A. Mittiga, *Phys. Status Solidi*, 2016, **13**, 35–39.
21 Y. Nouri, B. Hartiti, A. Batan, A. Ziti, H. Labrim, A. Ouannou, A. Laazizi, S. Fadili, M. Tahri and P. Thévenin, *Opt. Mater.*, 2023, **137**, 113602.
22 L. L. Baranowski, P. Zawadzki, S. Christensen, D. Nordlund, S. Lany, A. C. Tamboli, L. Gedvilas, D. S. Ginley, W. Tumas and E. S. Toberer, *Chem. Mater.*, 2014, **26**, 4951–4959.
23 A. Shigemi, T. Maeda and T. Wada, *Phys. Status Solidi*, 2015, **252**, 1230–1234.

24 C. Li, H. Song, Y. Cheng, R. Qi, R. Huang, C. Cui, Y. Wang, Y. Zhang and L. Miao, *ACS Appl. Energy Mater.*, 2021, **4**, 8728–8733.
25 S. Nakamura, H. Funabiki and S. Shiga, *Phys. Status Solidi C*, 2017, **14**, 1600172.
26 K. Lohani, H. Nautiyal, N. Ataollahi, C. Fanciulli, I. Sergueev, M. Etter and P. Scardi, *J. Phys. Chem. C*, 2020, **125**, 178–188.
27 J. B. Raval, S. H. Chaki, B. S. Shah and M. P. Deshpande, *Mater. Today: Proc.*, 2023, **73**(Part 4), 562–566.
28 S. Petrosyan, A. Musayelyan, E. Zaretskaya, V. Gremenok, K. Buskis and A. Stanchik, *Chalcogenide Lett.*, 2023, **20**, 811–820.
29 S. Rabaoui, H. Dahman, S. Dekhil, K. Omri, A. Alyamani and L. El Mir, *J. Mater. Sci.:Mater. Electron.*, 2015, **26**, 8588–8594.
30 Y. Igarashi, T. Tomono, K. Tanaka and K. Moriya, *Jpn. J. Appl. Phys.*, 2022, **61**, SB1002.
31 J. Raval, B. Shah, D. Kumar, S. H. Chaki and M. P. Deshpande, *Chem. Eng. Sci.*, 2024, 119728.
32 A. Kanai, K. Toyonaga, K. Chino, H. Katagiri and H. Araki, *Jpn. J. Appl. Phys.*, 2015, **54**, 08KC06.
33 J. Li, C. Xue, Y. Wang, G. Jiang, W. Liu and C. Zhu, *Sol. Energy Mater. Sol. Cells*, 2016, **144**, 281–288.
34 M. Nakashima, J. Fujimoto, T. Yamaguchi and M. Izaki, *Appl. Phys. Express*, 2015, **8**, 42303.
35 A. Kanai and M. Sugiyama, *Sol. Energy Mater. Sol. Cells*, 2021, **231**, 111315.
36 S. S. Bal, A. Basak and U. P. Singh, *Opt. Mater.*, 2022, **127**, 112282.
37 D. Roy, R. Garain, A. Basak, S. Behera, R. Patel and U. P. Singh, in *Recent Advances in Power Systems: Select Proceedings of EPREC 2022*, Springer, 2023, pp. 63–75.
38 A. Siddique, M. Nurul Islam, H. Karmaker, A. K. M. Asif Iqbal, A. Al Mazed Khan, M. Aminul Islam and B. Kumar Das, *Results Opt.*, 2024, **16**, 100713.
39 M. J. Nayeen, B. K. Mondal, S. R. Basu and J. Hossain, *Sol. Energy*, 2023, **265**, 112076.
40 S. E. Lachhab, A. Bliya, K. Nabaoui, E. Al Ibrahmi and L. Dlimi, *Aust. J. Electr. Electron. Eng.*, 2024, **21**, 29–35.
41 S. M. Yadav and A. Pandey, *Mater. Res. Innov.*, 2023, **27**, 503–510.
42 M. R. Butaev, V. I. Kozlovsky and Y. K. Skasyrsky, *Opt. Laser Technol.*, 2023, **158**, 108890.
43 S. I. S. Mashuri, M. F. Kasim, N. H. M. Kaus, Y. H. Tan, A. Islam, U. Rashid, N. Asikin-Mijan, J. Andas, Y. H. Taufiq-Yap and M. K. Yaakob, *Renewable Sustainable Energy Rev.*, 2023, **184**, 113602.
44 M. Kamalian, E. Hasani, L. B. Habashi and M. G. Arashti, *Phys. Rev. B: Condens. Matter Mater. Phys.*, 2024, **674**, 415524.
45 A. A. Faremi, P. A. Olubambi, A. O. Salau and A. A. Ibiyemi, *Results Eng.*, 2023, **18**, 101039.
46 E. Ö. Alagöz, H. Jahangiri and S. Kaya, *Mater. Adv.*, 2024, **5**, 1513–1522.
47 M. D. A. H. Pappu, A. Kuddus, B. K. Mondal, A. T. Abir and J. Hossain, *Opt. Continuum*, 2023, **2**, 942–955.
48 R. V Ingle, S. F. Shaikh, J. Kaur, M. Ubaidullah, B. Pandit and H. M. Pathan, *Mater. Sci. Eng., B*, 2023, **294**, 116487.
49 J. A. Melchor-Robles, K. E. Nieto-Zepeda, N. E. Vázquez-Barragán, M. Arreguín-Campos, K. Rodríguez-Rosales, J. Cruz-Gómez, A. Guillén-Cervantes, J. Santos-Cruz, M. D. L. L. Olvera and G. Contreras-Puente, *Coatings*, 2024, **14**, 452.
50 P. M. Perillo and D. F. Rodriguez, *Phys. Rev. B: Condens. Matter Mater. Phys.*, 2024, **680**, 415828.
51 D. Kumar, C. Lal, D. Veer, D. Singh, P. Kumar and R. S. Katiyar, *Mater. Lett.:X*, 2023, **18**, 100204.
52 R. I. Jasim, E. H. Hadi, S. S. Chiad, N. F. Habubi, M. Jadan and J. S. Addasi, *J. Ovonic Res.*, 2023, **19**, 187.
53 W. Ho and C. Y. Jimmy, *J. Mol. Catal. A: Chem.*, 2006, **247**, 268–274.
54 R. S. Singh, S. Bhushan, A. K. Singh and S. R. Deo, *Dig. J. Nanomater. Biostructures*, 2011, **6**, 403.
55 D. Parajuli, K. C. Devendra, K. B. Khattri, D. R. Adhikari, R. A. Gaib and D. K. Shah, *Sci. Rep.*, 2023, **13**, 12193.
56 M. Belaqziz, K. Medjnoun, K. Djessas, H. Chehouani and S. E. Grillo, *Mater. Res. Bull.*, 2018, **99**, 182–188.
57 P. Scherrer, *Nach Ges Wiss Gottingen*, 1918, **2**, 8–100.
58 J. Il Langford and A. J. C. Wilson, *Appl. Crystallogr.*, 1978, **11**, 102–113.
59 V. Uvarov and I. Popov, *Mater. Charact.*, 2007, **58**, 883–891.
60 A. R. Machale, H. D. Shelke, S. A. Phaltane and L. D. Kadam, *Chem. Phys. Lett.*, 2022, **808**, 140097.
61 S. H. Chaki, M. P. Deshpande and J. P. Tailor, *Thin Solid Films*, 2014, **550**, 291–297.
62 S. M. H. Al-Jawad, M. Rasheed and Z. Y. Abbas, *J. Opt.*, 2024, 1–22.
63 S. R. Patel, S. H. Chaki, S. V Bhatt, M. P. Deshpande, S. S. Soni and S. N. Bariya, *Thin Solid Films*, 2024, **791**, 140242.
64 T. S. Reddy and M. C. S. Kumar, *J. Ovonic Res.*, 2019, **15**(6), 365–376.
65 S. Dias and S. B. Krupanidhi, *AIP Adv.*, 2016, **6**, 25217.
66 S. Dias and S. B. Krupanidhi, *Mater. Res. Express*, 2016, **3**, 105006.
67 S. Dias, S. Chirakkara, N. Patel and S. B. Krupanidhi, *J. Mater. Sci.:Mater. Electron.*, 2018, **29**, 2131–2139.
68 S. Dias, K. Kumawat, S. Biswas and S. B. Krupanidhi, *Inorg. Chem.*, 2017, **56**, 2198–2203.
69 G. Hodes, *J. Phys. Chem. Lett.*, 2012, **3**, 1208–1213.
70 A. C. Lokhande, A. Shelke, P. T. Babar, J. Kim, D. J. Lee, I.-C. Kim, C. D. Lokhande and J. H. Kim, *RSC Adv.*, 2017, **7**, 33737–33744.
71 T. A. Kuku and O. A. Fakolujo, *Sol. Energy Mater.*, 1987, **16**, 199–204.
72 Y. Nosaka and A. Y. Nosaka, *J. Phys. Chem. Lett.*, 2016, **7**, 431–434.
73 A. Panepinto, A. Krumpmann, D. Cornil, J. Cornil and R. Snyders, *Appl. Surf. Sci.*, 2021, **563**, 150274.
74 M. Abdelfatah, W. Ismail, N. M. El-Shafai and A. El-Shaer, *Mater. Technol.*, 2021, **36**, 712–720.

75 S. Thiruvenkadam, P. Sakthi, S. Prabhakaran, S. Chakravarty, V. Ganesan and A. L. Rajesh, *Phys. Rev. B: Condens. Matter Mater. Phys.*, 2018, **538**, 8–12.
76 M. Nakashima, T. Yamaguchi, H. Itani, J. Sasano and M. Izaki, *Phys. Status Solidi*, 2015, **12**, 761–764.
77 Y. Wang, J. Li, C. Xue, Y. Zhang, G. Jiang, W. Liu and C. Zhu, *J. Mater. Sci.*, 2017, **52**, 6225–6234.
78 S. Sikiru, T. L. Oladosu, T. I. Amosa, S. Y. Kolawole and H. Soleimani, *J. Energy Storage*, 2022, **53**, 105200.
79 H. Dahman, S. Rabaoui, A. Alyamani and L. El Mir, *Vacuum*, 2014, **101**, 208–211.
80 M. R. Pallavolu, R. R. Nallapureddy, S. W. Joo and C. Park, *Opt. Mater.*, 2021, **111**, 110668.
81 A. El-Shaer, S. Ezzat, M. A. Habib, O. K. Alduaij, T. M. Meaz and S. A. El-Attar, *Crystals*, 2023, **13**(5), 788.
82 L. N. Ibrahimova, N. M. Abdullayev, S. R. Azimova and Y. I. Aliyev, *East Eur. J. Phys.*, 2024, 293–296.
83 X. Liu, A. Abbas, M. Togay, V. Kornienko, R. Greenhalgh, K. Curson, J. Bowers, K. Barth, M. Walls and E. Bastola, *Sol. Energy Mater. Sol. Cells*, 2024, **267**, 112717.
84 V. Gadore, S. R. Mishra and M. Ahmaruzzaman, *Sci. Rep.*, 2023, **13**, 7708.
85 W. Ismail, G. Ibrahim, M. A. Habib, O. K. Alduaij, M. Abdelfatah and A. El-Shaer, *Nanomaterials*, 2023, **13**, 1764.
86 Z. Ju, X. Qi, S. Schaefer, M. R. McCartney, D. J. Smith, A. V. G. Chizmeshya, T. McCarthy, A. McMinn, S. Grover and Y.-H. Zhang, *IEEE J. Photovoltaics.*, 2024, **14**(5), 752–757.
87 M. H. Huseynaliyev and L. N. Ibrahimova, Optical Properties Of Cdse Thin Films Produced By The Cbd Method From Four-Component And Three-Component Solutions.
88 E. Singh and H. S. Nalwa, *RSC Adv.*, 2015, **5**, 73575–73600.
89 B. Patel, R. K. Pati, I. Mukhopadhyay and A. Ray, *J. Anal. Appl. Pyrolysis*, 2018, **136**, 35–43.
90 O. Z. Sharaf and M. F. Orhan, *Renewable Sustainable Energy Rev.*, 2015, **50**, 1500–1565.
91 B. Y. Taher and A. S. Ahmed, *Chalcogenide Lett.*, 2021, **18**, 717–724.
92 M. F. A. Alias, B. Y. Taher, I. S. Naji, S. Iqbal, A. Kayani, M. F. Mabrook and A. A. J. Al-Douri, *Chalcogenide Lett.*, 2019, **16**(12), 577–586.
93 M. He, A. C. Lokhande, I. Y. Kim, U. V. Ghorpade, M. P. Suryawanshi and J. H. Kim, *J. Alloys Compd.*, 2017, **701**, 901–908.
94 M. H. Sayed, E. V. C. Robert, P. J. Dale and L. Gütay, *Thin Solid Films*, 2019, **669**, 436–439.
95 M. W. Dlamini, M. S. G. Hamed, X. G. Mbuyise and G. T. Mola, *J. Mater. Sci.:Mater. Electron.*, 2020, **31**, 9415–9422.
96 N. Romeo, A. Bosio, V. Canevari and A. Podestà, *Sol. Energy*, 2004, **77**, 795–801.
97 H.-J. Du, W.-C. Wang and J.-Z. Zhu, *Chin. Phys. B*, 2016, **25**, 108802.
98 R. Hosen, S. Sikder, M. S. Uddin, M. M. Haque, H. Mamur, M. R. A. Bhuiyan and J. Alloy, *Metall. Syst.*, 2023, **4**, 100041.
99 S. B. Jathar, S. R. Rondiya, Y. A. Jadhav, D. S. Nilegave, R. W. Cross, S. V Barma, M. P. Nasane, S. A. Gaware, B. R. Bade, S. R. Jadkar, A. M. Funde and N. Y. Dzade, *Chem. Mater.*, 2021, **33**, 1983–1993.
100 H. D. Shelke, A. C. Lokhande, J. H. Kim and C. D. Lokhande, *J. Colloid Interface Sci.*, 2017, **506**, 144–153.
101 S. P. Meenakshisundaram and M. B. Sridharan, *J. Alloys Compd.*, 2024, **981**, 173734.
102 P. Singh and N. M. Ravindra, *Sol. Energy Mater. Sol. Cells*, 2012, **101**, 36–45.
103 D. Das, P. Kalita and O. Roy, *Renewable Sustainable Energy Rev.*, 2018, **84**, 111–130.
104 G. Bakan, N. Khan, H. Silva and A. Gokirmak, *Sci. Rep.*, 2013, **3**, 2724.
105 R. K. Ahrenkiel, in *Semiconductors and Semimetals*, Elsevier, 1993, vol. 39, pp. 39–150.
106 P. Löper, D. Pysch, A. Richter, M. Hermle, S. Janz, M. Zacharias and S. W. Glunz, *Energy Procedia*, 2012, **27**, 135–142.
107 R. N. Pandey, K. S. C. Babu and O. N. Srivastava, *Prog. Surf. Sci.*, 1996, **52**, 125–192.
108 F. A. Lindholm, J. J. Liou, A. Neugroschel and T. W. Jung, *IEEE Trans. Electron Devices*, 1987, **34**, 277–285.
109 R. H. Sardar, A. Bera, S. Chattopadhyay, S. I. Ali, S. Pramanik and A. C. Mandal, *Opt. Mater.*, 2024, **155**, 115818.
110 I. S. Amiri, H. Ahmad, M. M. Ariannejad, M. F. Ismail, K. Thambiratnam, M. Yasin and N. M. A. Nik Abdul-Aziz, *Surf. Rev. Lett.*, 2016, **24**, 1750073.
111 A. S. Mathur, S. Upadhyay, P. P. Singh, B. Sharma, P. Arora, V. K. Rajput, P. Kumar, D. Singh and B. P. Singh, *Opt. Mater.*, 2021, **119**, 111314.
112 M. Ali, M. A. Abedin, M. S. Hossain and E. S. Hossain, *Chalcogenide Lett.*, 2020, **17**, 85–98.